Self-Aligning Nanojunctions for Integrated Single-Molecule Circuits

Bo Liu[1], Busra Demir[2,3], Caglanaz Akin Gultakti[2,3], Jonathan D. Marrs[4], Ersin Emre Oren[2,3], Joshua Hihath[1,4,5,*]

[1] *Biodesign Center for Bioelectronics and Biosensors at Arizona State University, Tempe, AZ 85287, USA*

[2] *Bionanodesign Laboratory, Department of Biomedical Engineering, TOBB University of Economics and Technology, Ankara, 06560, Türkiye*

[3] *Department of Materials Science and Nanotechnology Engineering, TOBB University of Economics and Technology, Ankara 06560, Türkiye*

[4] *Department of Electrical and Computer Engineering, University of California, Davis. Davis, CA 95616, USA*

[5] *School of Electrical, Computer, and Energy Engineering Arizona State University, Tempe, AZ 85287, USA*

*Corresponding author. Email: jhihath@asu.edu

Robust, high-yield integration of nanoscale materials such as graphene nanoribbons, nanoparticles, or single-molecules with conventional electronic circuits has proven to be challenging.[1–5] This difficulty arises because the contacts to these nanomaterials must be precisely fabricated with angstrom-level resolution to make reliable connections, and at manufacturing scales this cannot be achieved with even the highest-resolution lithographic tools.[6–8] Here we introduce an approach that circumvents this issue by precisely synthesizing nanometer-scale gaps between metallic electrodes using a self-aligning, solution-phase process, which allows facile integration with conventional electronic systems with yields approaching 50%. The electrode separation is controlled by covalently binding metallic single-walled carbon nanotube (mCNT) electrodes to individual DNA duplexes to synthesize hybrid mCNT-DNA-mCNT nanojunctions, where the gap is precisely matched to the DNA length. Upon integration, the resulting single-molecule circuits have electronic properties dominated by the DNA in the junction, have reproducible conductance values with low dispersion, and are stable and robust enough to be utilized as active, high-specificity electronic biosensors for dynamic single-molecule detection of specific oligonucleotides, such as those related to the SARS-CoV-2 genome. This scalable approach for high-yield integration of nanometer-scale materials will create new opportunities for manufacturing hybrid electronic systems for a wide range of applications.

The development of self-aligning transistors, where the gate electrode is used as a mask layer to pattern the source and drain, was a key breakthrough that greatly improved the manufacturing yield for semiconductors and enabled the continued scaling of electronic systems over many device generations.[9,10] Now, in recent decades a variety of novel low-dimensional materials have been developed with unique electronic properties, including CNTs,[11,12] semiconductor nanowires,[13] graphene and other 2D materials,[14,15] and molecular electronic components.[16] However, despite the promise of these systems, the ability to manufacture these materials into functional and reproducible devices at-scale, and to integrate them into larger-scale lithography processes has remained challenging.[17,18] This issue becomes increasingly prominent as the size-scale decreases to nanometer and molecular levels.[4,7] For example, while an incredible variety of novel, molecularly-enabled electronic functions have been demonstrated including quantum interference,[8,19] neuromorphic and memristive activity,[20–22] and optoelectronic control,[23] the utility of these devices has been restricted to understanding physical and chemical processes at the nanoscale due to the difficulties with larger-scale integration.[2,24,25] To realize the full utility of these systems they must be incorporated into stable, robust, and reliable electronic systems. Thus, inspired by the techniques used for creating self-aligned transistors, we present a method for utilizing controlled, bottom-up self-assembly processes to create hybrid nanomaterials in solution-phase, and combine it with top-down lithographic techniques to create self-aligning single-molecule devices, where the molecule itself is used to define the gap between metallic electrodes, with an overall yield of 44.6% (Fig. 1). We demonstrate the functionality, stability, and inherent single-molecule nature of this approach by creating a dynamic, high signal-to-noise ratio (SNR), electronic single-molecule biosensor capable of identifying specific oligonucleotide sequences with high fidelity. This approach provides a basis for developing reliable methods for integrating single-molecule circuits with conventional electronic systems to allow the unique functionality of molecular systems to be harnessed at scale.

To create robust, self-aligned single-molecule junctions we use mCNTs to synthesize hybrid mCNT-molecule-mCNT nanojunctions in solution phase. This hybrid system ensures that the gap between the two mCNTs is atomically matched to the length of the interconnecting molecule. Such a feat is exceedingly difficult with conventional lithography,[1,3,5] but by harnessing the inherent strengths of chemical control within molecular systems, this solution-phase approach allows facile junction self-alignment. In these hybrid junctions we utilize only metallic CNTs to improve the

reproducibility and decrease the dispersion of the conductance properties. DNA is selected as an initial molecular target due to its extensively studied electronic properties, and its potential utility as a biosensing element.[26,27]

To synthesize the mCNT-DNA-mCNT nanojunctions we begin with commercially available mCNTs that are soluble in aqueous solutions.[28] To protect the mCNT sidewalls during the impending chemical processes, they are coated with single-stranded $(GT)_{20}$ DNA (Fig. 1a,b), which binds strongly to the DNA through noncovalent interactions and ensures the continued solubility of the mCNTs in aqueous phases.[29–32] After this step (see SI Methods), the DNA wrapped-mCNTs are added to a solution of the target DNA duplexes that are terminated on both ends with an amine group ($-(CH_2)_6-NH_2$). Then, an amidation reaction between the terminal amines and the exposed carboxylic acid groups on the ends of the mCNTs is initiated using hexafluorophosphate azabenzotriazole tetramethyl uronium (HATU) to synthesize the final structure (Fig. 1a,b).[33]

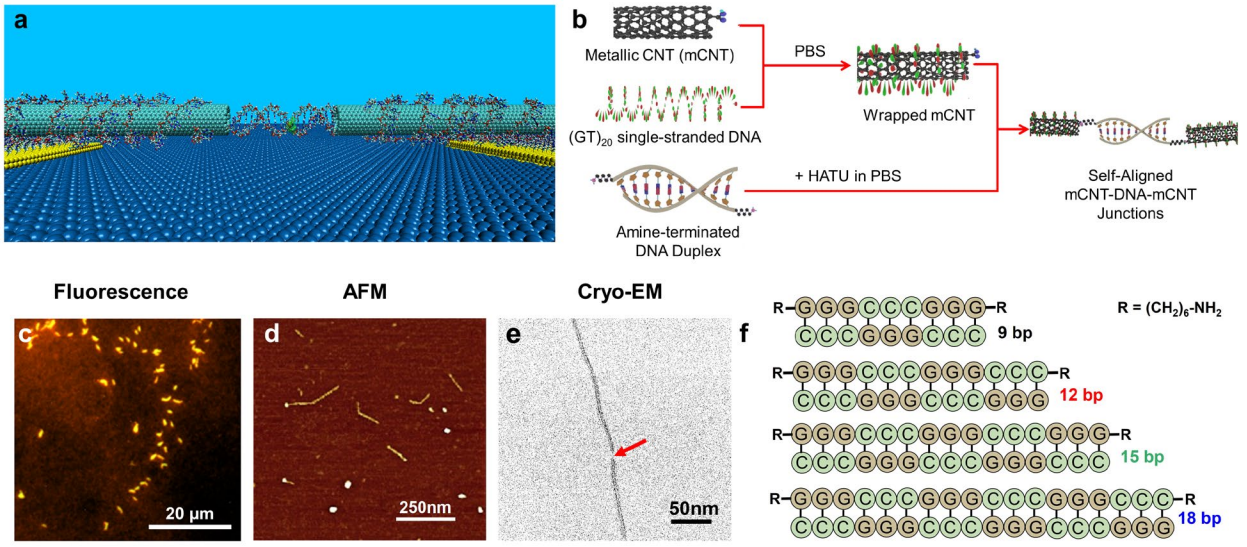

Fig. 1. Development of hybrid mCNT-DNA-mCNT nanojunctions. a) Schematic of final circuit implementation with a mCNT-DNA-mCNT junction between two gold electrodes that are coated with cystamine. b) Two-step reaction process for synthesizing self-aligning mCNT-DNA-mCNT nanohybrids, carboxyl-terminated mCNT are wrapped with (GT)20, then coupled to amino-functionalized DNA oligonucleotides in PBS buffer. c) Fluorescence micrograph of mCNT-DNA-mCNT. d) Atomic force microscope image of mCNT-DNA-mCNT structures on a mica surface. e) Cryo-EM micrograph of mCNT-DNA-mCNT devices, a ~3 nm gap is highlighted between mCNT structures. f) Series of alternating G:C triplet DNA sequences studied within the gap region.

To examine the morphological properties of these potential mCNT-DNA-mCNT structures we first utilize fluorescence microscopy. By incubating the samples with ethidium bromide (EtBr) and

comparing the resulting fluorescence images (Fig. 1c) with control experiments (Fig. S1), we find that the combination of single-stranded DNA wrapping and amidation with DNA results in structures that have either single or multiple bends in the backbone, indicative of a linked structure with differing persistence lengths.[34,35] These results are further corroborated by atomic force microscopy (AFM) images where V-shaped features commonly appear (Fig. 1d). The AFM images reveal that the resulting structures are typically on the order of 250-350 nm and that there are often locations within the structures that possess a smaller cross-section than the rest of the structures (Fig. S2). However, it is difficult to determine whether these features are due to the presence of single-molecules between two mCNTs or due to defects in the single-stranded DNA wrapping process. Thus, to further investigate this possibility, we utilize cryogenic transmission electron microscopy (cryo-EM) to examine the structures. The cryo-EM images indicate that gaps appear in the mCNT structures (Fig. 1e), which is again indicative of the formation of mCNT-DNA-mCNTs. Taken together these characterization approaches consistently suggest molecularly aligned mCNT-DNA-mCNT structures are formed using the above procedure.

Next, to demonstrate the single-molecule nature of these nanomaterials more conclusively, we turn to electrical characterization techniques. We start by analyzing the electrical properties of a 12 bp sequence with alternating G:C triplets (5'-GGG CCC GGG CCC-3' + complement) with amine linkers on each end (Fig. 1f). To create the circuits for electrical characterization, we incubated a microfabricated substrate with 300 nm gap Au electrodes that are coated with a cysteamine monolayer in the mCNT-DNA-mCNT solution (see SI for details). Fig. 2a plots 100 I-V characteristics from a single, bridged 300 nm gap measured in a 100 mM sodium phosphate buffer solution (PBS) at room temperature. For bias voltages swept over a ±0.5 V range, the I-V curves of the 12 bp nanojunction are nearly linear indicating ohmic transport behavior. And, as can be seen by the reproducibility of the I-V characteristics and the time series measurements on these devices (Fig. 2b), the structures and conductance values are very stable over time.

To examine the reproducibility of the measured conductance values, we examined 58 pairs of 300 nm gap devices across three different chips, and the data from each of these gaps is plotted in Fig. 2c. There are primarily three different conductance regimes visible in this plot. The grey region shows gaps that are open circuits, indicating no bridging occurred. The yellow region includes high-conductance values. These electrode pairs are either short-circuited during fabrication or bridged by mCNTs or bundled structures. The third, pink region, which spans a

conductance range of $1x10^{-4\pm1}$ G_0 (where G_0 is the conductance quantum, G_0 = = 77.48 μS), displays a series of devices with a narrow conductance distribution at $1.02\times10^{-4} \pm 0.17\times10^{-4}$ G_0, which is in close agreement with published values for this sequence obtained using the break junction approach.[36] Scanning electron microscopy (SEM) images of the devices from this conductance range verify that they are bridged by a single entity (Fig. 2d). Notably, of the 58 electrode pairs measured 45% (26 devices) have a conductance value within this window.

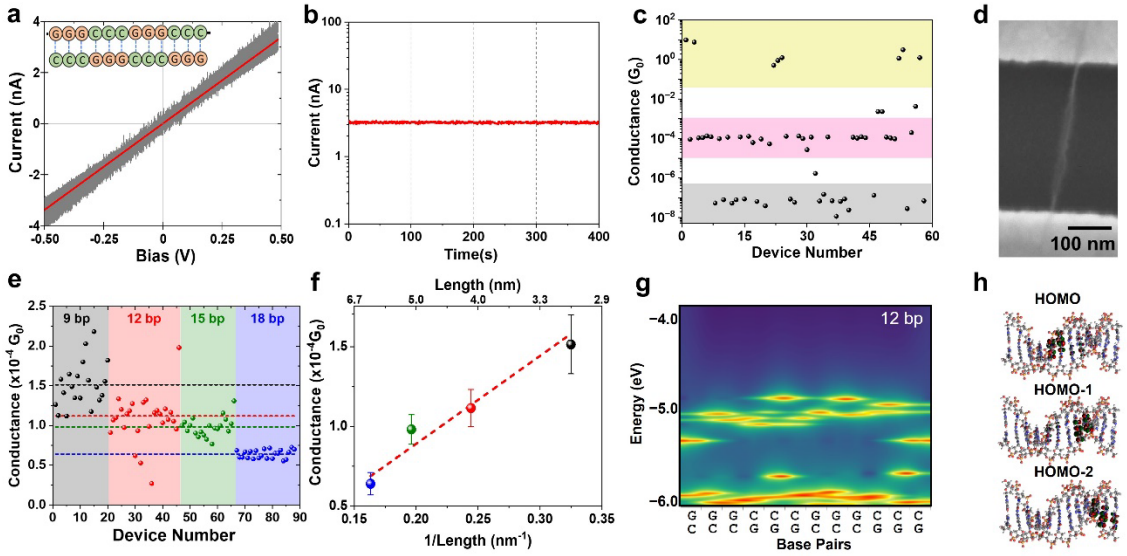

Fig. 2. Charge transport properties of hybrid mCNT-DNA-mCNT nanojunctions. a) 100 repeated I-V characteristics (gray background) for the 12 bp G:C sequence shown in the inset and a linear fitting to the data (R^2= 0.989, red line) indicating ohmic transport. b) Current through the device shown in (a) over a 400 s time period. c) Aggregated data from 58 300 nm gap devices with the 12 bp sequence. There are 3 distinctive regimes: high conductance (> 10^{-1} G_0, yellow), medium conductance ($1x10^{-4\pm1}$ G_0, pink), and low conductance (< 10^{-6} G_0, gray). 45% of the devices have a conductance in the pink region. d) SEM image of one of the devices in the pink region of (c) showing a single bridge between the electrodes. e) Plot of all devices with a conductance in the range of $1x10^{-4\pm1}$ G_0 for all 4 G:C triplet sequences studied from 9-18 bp, and their average values (dashed lines). f) Conductance of the G:C triplet sequences vs. 1/L. The linear dependence of the conductance indicates a hopping-dominated transport mechanism. Error bars are standard deviations calculated from all measurements in plot (e). g) 2D density of states plot for the 12 bp sequence showing a series of delocalized states in a narrow energy range. h) Iso-plots for the 3 highest occupied molecular orbitals (HOMO) demonstrating orbitals are delocalized over several bases.

Upon verifying that the measured conductance values stem from individual bridges between the electrodes, the next step is to demonstrate that these conductance values are determined by mCNT-DNA-mCNT-based single-molecule junctions. To do so we take advantage of the self-

alignment capabilities of this approach, and systematically measure the conductance of these alternating G:C triplet sequences with lengths of 9, 12, 15, and 18 base pairs. As seen in Fig. 2e the conductance of each of these molecules falls in a narrow region around $1x10^{-4}$ G_0, which is consistent with previous measurements on GC-rich DNA using Au electrodes.[37,38] Moreover, it is also apparent that there is a systematic decrease in the conductance with increasing length (L), and we find that this change in conductance is directly proportional to 1/L (Fig. 2f). This linear dependence of the conductance on length is indicative of a hopping-based transport mechanism, which has been widely attributed to GC-rich sequences.[39,40] We note that if the DNA was not playing a role in the conductance of these systems, we would expect no length dependence of the conductance because the nominal electrode gap is 300 nm in all cases. Thus, these measurements provide a clear indication that the circuits are derived from single-molecule junctions. Altogether, from the four molecules, we measured 197 electrode pairs and obtained an overall yield of 44.6% (88 bridged gaps).

To examine hopping as the transport mechanism, we performed molecular dynamics (MD) simulations, density functional theory (DFT) electronic structure calculations, and extracted the density of states for the system.[26,41] As can be seen in Fig. 2g,h, for the 12 bp case, the top several occupied molecular orbitals are delocalized over several guanines in the G-triplet regions (see SI Fig. S4 for other molecules). We also find a relatively weak coupling between the triplets (average of 7.5 meV), indicating that a charge would likely traverse these structures by systematically hopping between delocalized energy levels.

Finally, to unambiguously verify the single-molecule nature of these nanomaterial-based circuits, examine their stability, and determine their utility to serve as active electronic components, we utilize the system to create single-molecule electronic biosensors (Fig. 3). For these experiments, we test whether we can detect the presence of a specific oligonucleotide related to D614G mutation (aspartic acid swapped for glycine at amino acid residue 614 on the spike protein) of the SARS-CoV-2 virus. The D614G modification was an early mutation that greatly increased the virulence of SARS-CoV-2,[42,43] and by focusing on this coding sequence with a known point mutation difference between the wild type (WT) (GAT codon) and the variant (GGT codon) we can examine the specificity of this detection approach, and its resilience when challenged with potentially interfering targets.

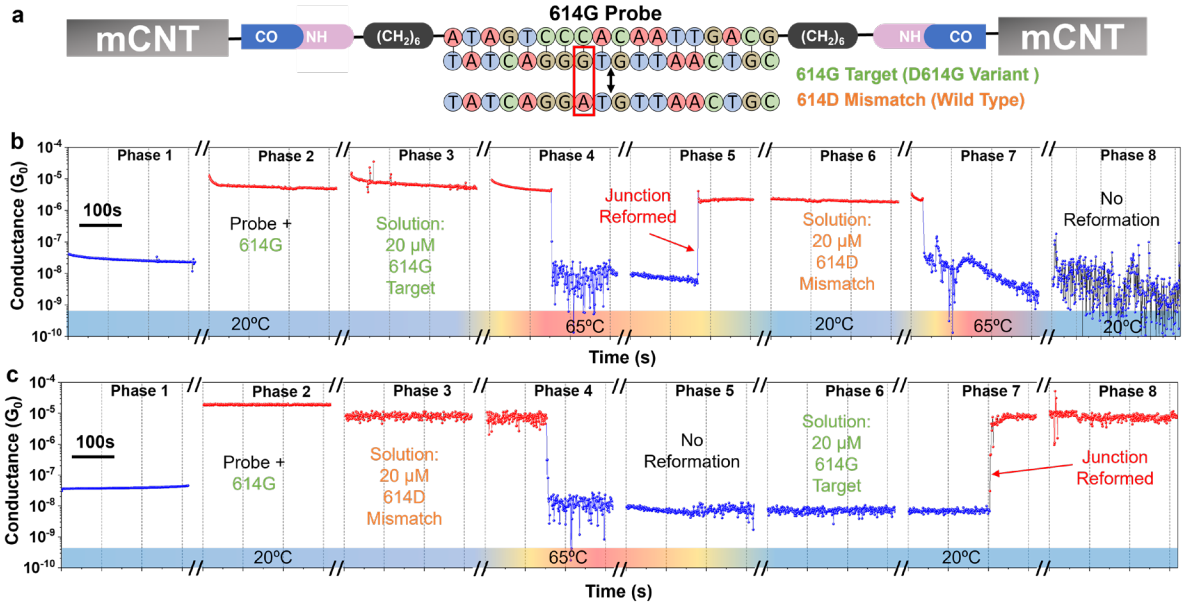

Fig. 3. Electronic oligonucleotide detection using hybrid mCNT-DNA-mCNT nanojunction based circuits. a) Schematic representation of the device with the 614G probe and target sequences (614G and 614D). b) Conductance vs. time for the mCNT-614G Probe-mCNT junction. Phase 1: open-circuit blank device; Phase 2: Conductance of 614G Probe/Target (PBS, 20°C); Phase 3: Replace solution with 20 µM 614G targets in PBS; Phase 4: Dehybridize the duplex by heating the system at a rate of 0.5°C/s, a conductance drop of 3 orders of magnitude indicates device breakdown; Phase 5: During cooling the junction is reformed when a 614G target from solution binds to the probe sequence. Phase 6: Replace solution with the mismatched 614D sequence (WT). Phase 7: Repeat dehybridization process by heating the sample. Phase 8: upon cooling no device formation was observed. c) Similar procedure as in b) on a second device, but with reversed sample injection order. Mismatched DNA does not rehybridize in the junction in either case, but the matched 614G sequence does.

For the detection process, we selected an 18 bp DNA sequence identical to the SARS-CoV-2 genome that included several bases on either side of the point mutation D614G, which we refer to as the 614G target sequence (Fig. 3a), and then use a complementary DNA strand with amine linkers on either end as a probe molecule (614G Probe). We then hybridize the probe and target and link it to mCNTs as above. This structure is then incubated on a microelectrode chip for 30 minutes before identifying a bridged device. For the device examined, the conductance was stable at ~6×10^{-6} G_0 (Fig. 3b, Phase 2). Then, to decrease the possibility of additional mCNT-DNA-mCNT junctions bridging the electrodes during the sensing process the CNT solution is replaced with 20 µM 614G targets in PBS, and the conductance remains close to the original value during this buffer exchange process (Fig. 3b, Phase 3). Then, to complete the sensor preparation we heat the system toward 90°C at a rate of 0.5°C/s to dehybridize the duplex within the junction. When

the temperature reaches ~65°C, which corresponds to the calculated melting temperature for this sequence (T_m = 64.4°C), the conductance suddenly dropped to the resolution of the current amplifier, indicating a breakdown of the device (Fig. 3b, Phase 4). Now, with the conductance at effectively zero, we aim to detect the target sequence in the solution. To do so, we decrease the temperature of the cell back toward room temperature, and within several minutes of cooling, there is a sharp, stepwise increase in the conductance (Fig. 3b, Phase 5), which returned to 2.3×10^{-6} G_0. This binary change in the conductance with the formation and breakdown of the system is an additional, clear indicator of a single-molecule binding process.[44,45]

Next, to gauge the specificity of the system and determine whether the binary conductance change occurs due to the molecule or due to changes in the overall bridged structure upon temperature cycling, we repeated this experimental procedure after replacing the 614G solution in the cell with a 20 μM concentration of the wild type, mismatched, 614D sequence in PBS. Upon heating, the device again broke down at ~65°C, but this time, upon cooling no clear device formation was observed (Fig. 3b, Phase 6-8). This obvious difference in conductance response between 614G and 614D indicates that the sensing platform is extremely sensitive to single nucleotide polymorphisms. To confirm this result, a complementary experiment is performed on a second device, but with the order of target injection reversed (Fig. 3c). In this case the junction conductance still decreases to zero upon heating, and again no junction formation occurred when cooling with an excess of 614D present in the solution (Fig. 3c, Phase 1-5). However, when the 614D solution was replaced with the perfectly matched 614G sequence (Fig. 3c, Phase 6-8), we again observed junction formation with a conductance of 4.8×10^{-6} G_0. We also note that the entire measurement process takes ~2 hours, demonstrating the long-time stability of these single-molecule junctions.

In conclusion, solution-phase self-alignment of hybrid mCNT-single-molecule-mCNT nanojunctions provides an ability to create dynamic yet stable single-molecule circuits that are easily integrated with conventional lithographic processes. This approach allows nanomaterials integration with yields on the order of 50% using only standard, low-resolution photolithography without the addition of low-throughput electron beam or focused ion beam lithography, which opens the door for manufacturing nanoscale electronic circuits based on single-molecules or other nanoscale materials. We show that the resulting sensors can reliably detect targeted sequences with very high SNRs and limited possibilities for false positives from interfering sequences. This target-

agnostic platform will allow DNA and RNA sequence detection to be implemented for a wide range of applications in biology, healthcare, and security, for examining the presence of and identifying pathogens, performing liquid biopsies, and tracking disease progression. Moreover, the straightforward chemistry for creating these self-aligning structures provides new opportunities for integrating other molecular systems with electronic platforms including proteins, catalysts, and molecules that undergo field-controllable reactions, as well as more conventional molecular electronic devices such as switches, molecular memory devices, and diodes.

Methods

Preparation of mCNT-DNA-mCNT nanostructures

Metallic single wall carbon nanotubes (mCNTs) were purchased from Nano Integris, Inc. Phosphate buffer solution (PBS) and hexafluorophosphate azabenzotriazole tetramethyl uronium (HATU) were purchased from Thermo Fisher Scientific. All other analytical-grade chemicals were purchased from Sigma Aldrich. All DNAs were obtained from Alpha DNA, sequences are listed in the SI.

The mCNT wrapping process is driven primarily by favorable interactions between the ssDNA bases and the mCNT due to van der Waals and hydrophobic interactions. 0.1 mL of the mCNT (1 mg/mL) solution was first diluted with 2.5 mL PBS, then 2.5 mL of 5 μM $(GT)_{20}$ was added. After overnight incubation at room temperature, the mixture was placed in a clean tube surrounded by ice for at least 2 hours under sonication (at the power level of 3W) and then centrifuged at 5000 rpm (Eppendorf 5415C) for 2 hours to remove insoluble material. Then supernatant was collected and diluted with DI water (MilliQ), the volume of $(GT)_{20}$-dispersed mCNT solutions was kept to 2mL.

To covalently attach DNA duplexes to $(GT)_{20}$ wrapped mCNTs we began with amino-terminated DNA prepared at a concentration of 5 μM in 2 mL of PBS buffer and mixed it with 2 mL $(GT)_{20}$ wrapped mCNTs and ~0.13 mM of Hexafluorophosphate Azabenzotriazole Tetramethyl Uronium (HATU, coupling agent). The mixture was left to react at room temperature for 3 hours under weak sonication. Subsequently, any insoluble material was removed via 15 mins centrifugation at 12000 rpm. The mCNT-DNA-mCNT hybrids were then extracted from the supernatant.

Single-molecule device fabrication

The microelectrode platform used for electrical tests of the nanostructures was fabricated using optical lithography. In brief, a Si/Si_3N_4 wafer was first spin-coated with hexamethyldisilazane (HMDS) as an adhesive layer, followed by PID controlled baking at 110°C for 1 min. Then microelectrodes were patterned on the wafer using photolithography with KL5302 Hi-Res Photoresist (Kem Lab). After ~15 s development in CD-26 (TMAH), the wafer was gently rinsed with DI water and blow-dried with nitrogen to stop the development process. Then a PETS-RIE plasma etcher was employed to etch ~65 nm trenches into the silicon nitride. A Cr(adhesive)/Au multilayer of thickness 10 nm/55 nm was deposited by an E-Beam evaporator. The sample was then immersed in MICROPOSIT™ Remover 1165 for 90 minutes, and ultrasonicated to lift off residual resist and metal. After that, a 100 nm thick Si_3N_4 insulating layer was deposited using plasma-enhanced chemical vapor deposition (PECVD), to cover the gold electrodes. Micron-sized windows for the probing and sensor areas were patterned using the same photolithography process used previously for the microelectrodes. Finally, a ~100 nm etch into the PECVD Si_3N_4-cover layer was performed using the Plasma-Therma RIE to open the windows and expose the gold electrodes in the desired areas.

To couple the mCNT-DNA-mCNT structures to the electrode surfaces we began by immersing the freshly made substrates in a 10 mM solution of cysteamine overnight. The substrates were then removed from the solution, gently rinsed with DI water, and dried with a stream of nitrogen gas. After device characterization (blank test), a silicone ring was mounted and sealed to sensor area as sample reservoir. Thereafter, the modified Au electrodes were reacted with the mCNT-DNA-mCNT nanostructures through the same amidation reaction in 100 mM PBS solution to covalently bridge the gaps.

Electrical Characterization

All the device characterizations were performed by using a Cascade Micromanipulator probe station equipped with the semiconducting parameter analyzer (Keithley 4200-SCS) at room temperature with a consistent moisture content (30%). For thermal cycling measurements, a PID-controlled heater stage (±0.01 °C) was employed to adjust the temperature (20°C-95°C) at a constant rate. Sample surface temperatures were monitored via an infrared thermometer (Fluke-561).

Current sampling measurements were conducted with 0.5 V bias, and at least 3 minutes of monitoring for each electrode. Voltammetry scans (-0.5 V~0.5 V) were conducted simultaneously.

Fluorescence

The fluorescence studies of the mCNT-DNA-mCNTs structures with an ethidium bromide (EtBr) intercalating agent were performed with a ZEISS Axio Imager Widefield Fluorescence Microscope. The stock solution of EtBr– nanohybrids was generally prepared in a PBS buffer (containing 1 μM mCNT-DNA-mCNTs and at pH 7.2) and incubated for 30 min at 25 °C before being casted upon microscope slide for imaging.

AFM

The sample solution was deposited onto a piece of mica. Then mica was baked at 60°C under vacuum for 30 mins and rinsed with water to desalt the mica surface. Tapping mode was used to acquire the images under ambient conditions using a Digital Instruments Multimode AFM.

Cryo-EM

Cryogenic electron microscopy (Cryo-EM) measurements were carried out using a ThermoFisher Titan Krios electron microscope (Hillsboro, OR). The samples for cryo-TEM were prepared by plunge freezing. 3 μL of the sample solution was applied to a graphene oxide coated lacey carbon grid (EMS, Hatfield, PA, USA) and then glow-discharged for 15 s with 15 mA current. A thin vicinal film of the CNT sample was formed by blotting with Whatman no. 1 filter paper for approximately 6 s, and the grid was immediately plunged in liquid ethane held at liquid nitrogen temperature. The grid was then transferred to a microscope. Images were recorded at an accelerating voltage of 300 keV and magnifications ranging from 11,500× to 50,000× using K2 summit DED camera in low-dose imaging mode, with the electron dose not exceeding 60 electrons/Angstrom sq. The magnifications resulted in final pixel sizes ranging from 1-3 Angstroms, and the typical value of the sample under focus ranged from 1-3 microns.

Molecular Dynamics Simulations

9, 12, 15, 18 base pair long DNA molecules are generated using AMBER Nucleic Acid Builder.

All structures are neutralized with Na^+ counterions and added into an octahedral water box which had a 15 Å cutoff from the DNA molecules.

First, water molecules and counterions were subjected to 500 steps of energy minimization, while DNA molecules were restrained with 50 kcal/mol force. Then, 5000 steps of energy minimization were applied to the whole system without any restraint on any molecule. Then, the system is heated to 300 K in NVT ensemble within 100 ps while a 50 kcal/mol restraint force was applied to the DNA molecules. Next, the system equilibrated for 100 ps while a 0.5 kcal/mol restraint force was applied only to the DNA molecules. Finally, the entire system was simulated in an NPT ensemble for 100 ns without any restraining force applied via the AMBER 16[46] pmemd CUDA module. For all simulations, bsc1[47] and TIP3P[48] force fields were used to describe DNA and water molecules as well as counterions respectively. The particle Mesh Ewald[49] algorithm was used for long-range electrostatic interactions and a cut-off value of 10 Å was used for the van der Waals interactions. The simulations were performed and recorded for every 2 fs, resulting in 50,000 conformations in each trajectory. All bonds with the hydrogen atoms were constrained using the SHAKE algorithm.[50]

To evaluate the electronic properties of each structure, we employ a RMSD based clustering algorithm using VMD software,[51] which categorizes the DNA conformations observed throughout the simulation time. A cutoff value of 1.75 Å RMSD was chosen to cluster the DNA structures. We select the centroid structures from the most populated cluster (top cluster) which have minimum RMSD difference from the rest of the conformations within the top cluster. Subsequently, energy minimization is performed on the selected structures to relax residual strains resulting from thermal fluctuations during molecular dynamics before quantum mechanical calculations.

DFT Calculations

To perform DFT calculations, water molecules and counterions are removed from the previously energy-minimized representative structures. The total charge of each system is set to -16, -22, -28 and -34 for 9, 12, 15 and 18 bp long DNA molecules, respectively. Then, the calculations are carried out using the Gaussian 16[52] software package with the B3LYP exchange-correlation function and 6-31G(d,p) basis set which provides a balance between memory requirements, computational time and accuracy.[53,54] Previous studies have demonstrated that the

electronic structure of biomolecules in vacuum exhibits a vanishing HOMO-LUMO gap.[55] As a result, the utilization of implicit or explicit solvation models is necessary. In this work, we assumed that the only effect of the solvent is to modify the equilibrium electronic structure of the DNA molecules, thus we used the implicit solvation method PCM (Polarizable Continuum Model), within the Gaussian 16 software.[52] Molecular orbitals are generated using the Avogadro software.[56]

Density of States Calculations

We obtain Fock (H_0) and Overlap (S_0) matrices from DFT calculations and employ a Löwdin transformation[57] to convert H_0 into a Hamiltonian, H , in an orthogonal basis set via the following equation:

$$H = S_0^{(-0.5)} H_0 S_0^{(-0.5)} \quad (1)$$

The diagonal elements of H matrix account for the energy levels of each atomic orbital, and the off-diagonal elements represent the coupling between these atomic orbitals.

The density of states (DOS) along the molecule in a given energy is calculated using Green's function method. First, we compute the retarded Green's function (G^r) as shown in Eq. (2).

$$[E - (H + i\eta)]G^r = I \quad (2)$$

where E is the energy, and H is the Hamiltonian defined in Eq. (1).

Next, we calculate DOS for each atom (m) by extracting the corresponding diagonal elements of the retarded Green's function as follows:

$$DOS(m, E) = \frac{Im(diag(G_m^r(E)))}{\pi} \quad (3)$$

For the 2D DOS plots, we sum up the DOS values of each atom for the corresponding nucleobase and energy.

Acknowledgments: Authors acknowledge funding support from the National Science Foundation Future Manufacturing Program, NSF-2036865, and M.P. Anantram, William Livernois, and Yonggang Ke for fruitful discussions.

Author contributions:

Bo Liu, fabricated devices, performed experiments, analyzed results, wrote manuscript.

Busra Demir, performed simulations, edited manuscript.

Caglanaz Akin Gultakti, performed simulations, edited manuscript.

Jonathan Marrs, fabricated devices, edited manuscript.

Ersin Emre Oren, oversaw and analyzed simulations, edited manuscript.

Joshua Hihath, conceived experiments, analyzed results, wrote manuscript.

Competing interests:

Authors declare that they have no competing interests.

Data and materials availability:

All data are available in the main text or the supplementary materials, raw data is available upon request.

Supplementary Materials

List of DNA Sequences used for experiments.

Fig. S1. Fluorescent microscopy images of self-aligning mCNT-DNA-mCNT nanohybrids.

Fig. S2. AFM image of a mCNT-DNA-mCNT nanohybrid.

Fig. S3. Analysis of mCNT-DNA-mCNT devices of different lengths. (9, 15, 18 bp duplexes).

Fig. S4. 2-dimensional DOS plots and corresponding iso-plots for alternating G:C triplets

References

1. Guo, X. F. ; *et al.* Covalently bridging gaps in single-walled carbon nanotubes with conducting molecules. *Science* **311**, 356–359 (2006).
2. Roy, S. *et al.* Direct Electrical Measurements on Single-Molecule Genomic DNA Using Single-Walled Carbon Nanotubes. *Nano Lett.* **8**, 26–30 (2007).
3. Porath, D., Bezryadin, A., de Vries, S. & Dekker, C. Direct measurement of electrical transport through DNA molecules. *Nat. Lond.* **403**, 635–638 (2000).
4. Lörtscher, E. Wiring molecules into circuits. *Nat. Nanotechnol.* **8**, 381–384 (2013).
5. Puebla-Hellmann, G., Venkatesan, K., Mayor, M. & Lörtscher, E. Metallic nanoparticle contacts for high-yield, ambient-stable molecular-monolayer devices. *Nature* **559**, 232–235 (2018).
6. Park, H. *et al.* Nanomechanical oscillations in a single-C60 transistor. *Nat. Lond.* **407**, 58–60 (2000).
7. Jia, C. *et al.* Covalently bonded single-molecule junctions with stable and reversible photoswitched conductivity. *Science* **352**, 1443–1445 (2016).
8. Gehring, P., Thijssen, J. M. & van der Zant, H. S. J. Single-molecule quantum-transport phenomena in break junctions. *Nat. Rev. Phys.* **1**, 381–396 (2019).
9. Chih-Tang, S. Evolution of the MOS transistor-from conception to VLSI. *Proc. IEEE* **76**, 1280–1326 (1988).
10. Bower, R. W. & Dill, R. G. Insulated gate field effect transistors fabricated using the gate as source-drain mask. in *1966 International Electron Devices Meeting* 102–104 (1966). doi:10.1109/IEDM.1966.187724.
11. Meyyappan, M. Carbon Nanotube-Based Chemical Sensors. *Small* **12**, 2118–2129 (2016).
12. Rao, R. *et al.* Carbon Nanotubes and Related Nanomaterials: Critical Advances and Challenges for Synthesis toward Mainstream Commercial Applications. *ACS Nano* **12**, 11756–11784 (2018).
13. Ren, Y. *et al.* Synthesis of orthogonally assembled 3D cross-stacked metal oxide semiconducting nanowires. *Nat. Mater.* **19**, 203–211 (2020).
14. Xu, M., Liang, T., Shi, M. & Chen, H. Graphene-Like Two-Dimensional Materials. *Chem. Rev.* **113**, 3766–3798 (2013).
15. Baringhaus, J. *et al.* Exceptional ballistic transport in epitaxial graphene nanoribbons. *Nature* **506**, 349–349 (2014).
16. Xin, N. *et al.* Concepts in the design and engineering of single-molecule electronic devices. *Nat. Rev. Phys.* **1**, 211–230 (2019).

17. Fuller, C. W. *et al.* Molecular electronics sensors on a scalable semiconductor chip: A platform for single-molecule measurement of binding kinetics and enzyme activity. *Proc. Natl. Acad. Sci.* **119**, e2112812119 (2022).

18. Goswami, S. *et al.* Decision trees within a molecular memristor. *Nature* **597**, 51–56 (2021).

19. Gunasekaran, S., Greenwald, J. E. & Venkataraman, L. Visualizing Quantum Interference in Molecular Junctions. *Nano Lett.* **20**, 2843–2848 (2020).

20. Li, H. B., Tebikachew, B. E., Wiberg, C., Moth-Poulsen, K. & Hihath, J. A Memristive Element Based on an Electrically Controlled Single-Molecule Reaction. *Angew. Chem. Int. Ed.* **59**, 11641–11646 (2020).

21. Goswami, S. *et al.* Charge disproportionate molecular redox for discrete memristive and memcapacitive switching. *Nat. Nanotechnol.* **15**, 380–389 (2020).

22. Wang, Y. *et al.* Dynamic molecular switches with hysteretic negative differential conductance emulating synaptic behaviour. *Nat. Mater.* **21**, 1403–1411 (2022).

23. Meng, L. *et al.* Side-group chemical gating via reversible optical and electric control in a single molecule transistor. *Nat. Commun.* **10**, 1450 (2019).

24. Wang, H. *et al.* Transducing methyltransferase activity into electrical signals in a carbon nanotube-DNA device. *Chem. Sci.* **3**, 62–65 (2012).

25. Sun, W. *et al.* Precise pitch-scaling of carbon nanotube arrays within three-dimensional DNA nanotrenches. *Science* **368**, 874–877 (2020).

26. Li, Y. *et al.* Detection and identification of genetic material via single-molecule conductance. *Nat. Nanotechnol.* **13**, 1167–1173 (2018).

27. Tsutsui, M. *et al.* Electrical Detection of Single Methylcytosines in a DNA Oligomer. *J. Am. Chem. Soc.* **133**, 9124–9128 (2011).

28. Arnold, M. S., Green, A. A., Hulvat, J. F., Stupp, S. I. & Hersam, M. C. Sorting carbon nanotubes by electronic structure using density differentiation. *Nat. Nanotechnol.* **1**, 60–65 (2006).

29. Hirayama, K. *et al.* Attachment of DNA-Wrapped Single-Walled Carbon Nanotubes (SWNTs) for a Micron-Sized Biosensor. *ACS Omega* **7**, 47148–47155 (2022).

30. Attanzio, A. *et al.* Carbon Nanotube-Quantum Dot Nanohybrids: Coupling with Single-Particle Control in Aqueous Solution. *Small* **13**, 1603042 (2017).

31. Zheng, M. *et al.* DNA-assisted dispersion and separation of carbon nanotubes. *Nat. Mater.* **2**, 338–342 (2003).

32. Zheng, M. Sorting Carbon Nanotubes. *Top. Curr. Chem.* **375**, 13 (2017).

33. Palma, M. *et al.* Controlled Formation of Carbon Nanotube Junctions via Linker-Induced Assembly in Aqueous Solution. *J. Am. Chem. Soc.* **135**, 8440–8443 (2013).

34. Oruc, B., Celik, S., Hayat Soytas, S. & Unal, H. DNA Directed Self-Assembly of Single Walled Carbon Nanotubes into Three-Way Junction Nanostructures. *ACS Omega* **3**, 4157–4162 (2018).

35. Freeley, M. *et al.* Site-Specific One-to-One Click Coupling of Single Proteins to Individual Carbon Nanotubes: A Single-Molecule Approach. *J. Am. Chem. Soc.* **139**, 17834–17840 (2017).

36. Alangari, M., Demir, B., Gultakti, C. A., Oren, E. E. & Hihath, J. Mapping DNA Conformations Using Single-Molecule Conductance Measurements. *Biomolecules* **13**, 129 (2023).

37. Artés, J. M., Li, Y., Qi, J., Anantram, M. P. & Hihath, J. Conformational gating of DNA conductance. *Nat. Commun.* **6**, 8870 (2015).

38. Xiang, L. *et al.* Intermediate Tunneling-Hopping Transport Regime in DNA Charge Transport. *Nat. Chem.* **7**, 221–226 (2015).

39. Lewis, F. D. *et al.* Direct Measurement of hole transport dynamics in DNA. *Nat. Lond.* **406**, 51–53 (2000).

40. Bixon, M. & Jortner, J. Charge Transport in DNA Via Thermally Induced Hopping. *J. Am. Chem. Soc.* **123**, 12556–12567 (2001).

41. Qi, J., Edirisinghe, N., Rabbani, M. G. & Anantram, M. P. Unified model for conductance through DNA with the Landauer-Buttiker formalism. *Phys. Rev. B Condens. Matter Mater. Phys.* **87**, 85404–85404 (2013).

42. Guo, C. *et al.* The D614G mutation redirects SARS-CoV-2 spike to lysosomes and suppresses deleterious traits of the furin cleavage site insertion mutation. *Sci. Adv.* **8**, eade5085 (2022).

43. Zhang, L. *et al.* SARS-CoV-2 spike-protein D614G mutation increases virion spike density and infectivity. *Nat. Commun.* **11**, 6013 (2020).

44. Haiss, W. *et al.* Precision control of single-molecule electrical junctions. *Nat. Mater.* **5**, 995–1002 (2006).

45. Tang, L. *et al.* Measuring conductance switching in single proteins using quantum tunneling. *Sci. Adv.* **8**, eabm8149 (2022).

46. D.A. Case R.M. Betz, D. S. C., T. E. Cheatham, III, T. A. Darden, R. E. Duke, T. J. Giese, H. Gohlke, A. W. Goetz, N. Homeyer, S. Izadi, P. Janowski, J. Kaus, A. Kovalenko, T. S. Lee, S. LeGrand, P. Li, T. Luchko, R. Luo, B. Madej, K. M. Merz, G. Monard, P. ,. J. T. Berryman. AMBER 2016. (2016).

47. Ivani, I. *et al.* Parmbsc1: a refined force field for DNA simulations. *Nat. Methods* **13**, 55–58 (2016).

48. Jorgensen, W. L., Chandrasekhar, J., Madura, J. D., Impey, R. W. & Klein, M. L. Comparison of simple potential functions for simulating liquid water. *J. Chem. Phys.* **79**, 926–935 (1983).

49. Darden, T., York, D. & Pedersen, L. Particle mesh Ewald: An N·log(N) method for Ewald sums in large systems. *J. Chem. Phys.* **98**, 10089–10092 (1993).

50. Miyamoto, S. & Kollman, P. A. Settle: An analytical version of the SHAKE and RATTLE algorithm for rigid water models. *J. Comput. Chem.* **13**, 952–962 (1992).

51. Humphrey, W., Dalke, A. & Schulten, K. VMD: Visual molecular dynamics. *J. Mol. Graph.* **14**, 33–38 (1996).

52. Frisch, M. J. *et al.* Gaussian 16 Revision C.01. (2016).

53. Russo, N., Toscano, M. & Grand, A. Theoretical determination of electron affinity and ionization potential of DNA and RNA bases. *J. Comput. Chem.* **21**, 1243–1250 (2000).

54. Cauët, E., Dehareng, D. & Liévin, J. Ab Initio Study of the Ionization of the DNA Bases: Ionization Potentials and Excited States of the Cations. *J. Phys. Chem. A* **110**, 9200–9211 (2006).

55. Rudberg, E. Difficulties in applying pure Kohn–Sham density functional theory electronic structure methods to protein molecules. *J. Phys. Condens. Matter* **24**, 072202 (2012).

56. Hanwell, M. D. *et al.* Avogadro: an advanced semantic chemical editor, visualization, and analysis platform. *J. Cheminformatics* **4**, 17 (2012).

57. D'Amato, J. L. & Pastawski, H. M. Conductance of a disordered linear chain including inelastic scattering events. *Phys. Rev. B* **41**, 7411–7420 (1990).